An Integrated Sensitivity-Uncertainty Quantification Framework for Stochastic Phase-Field Modeling of Material Damage

Eduardo A. Barros de Moraes[1] | Mohsen Zayernouri*[2,3] | Mark M. Meerschaert[3]

[1]Department of Computational Mathematics, Science, and Engineering, Michigan State University, East Lansing, Michigan

[2]Department of Mechanical Engineering, Michigan State University, East Lansing, Michigan

[3]Department of Statistics and Probability, Michigan State University, East Lansing, Michigan

Correspondence
*Mohsen Zayernouri, Department of Computational Mathematics, Science, and Engineering, Michigan State University, 428 S Shaw Ln, East Lansing, MI, 48824. Email: zayern@msu.edu

Summary

Materials accumulate energy around voids and defects under external loading, causing the formation of micro-cracks. With increasing or repeated loads, those micro-cracks eventually coalesce to form macro-cracks, which in a brittle material can cause catastrophic failure without apparent permanent deformation. At the continuum level, a stochastic phase-field model is employed to simulate failure through introducing damage and fatigue variables. The damage phase-field is introduced as a continuous dynamical variable representing the volumetric portion of fractured material and fatigue is treated as a continuous internal field variable to model the effects of micro-cracks arising from energy accumulation. We formulate a computational-mathematical framework for quantifying the corresponding model uncertainties and sensitivities in order to unfold and mitigate the salient sources of unpredictability in the model, hence, leading to new possible modeling paradigms. Considering an isothermal isotropic linear elastic material with viscous dissipation under the hypothesis of small deformations, we employed Monte Carlo and Probabilistic Collocation methods to perform the forward uncertainty propagation, in addition to local-to-global sensitivity analysis. We demonstrate that the model parameters associated with free-energy potentials contribute significantly more to the total model output uncertainties, motivating further investigations for obtaining more predictable model forms, representing the damage diffusion.

KEYWORDS:
Thermodynamically consistent fatigue modeling, probabilistic collocation method, complex-step differentiation, global/local sensitivity analysis, crack propagation, model form/parameter uncertainty

1 | INTRODUCTION

Companies want to deliver safe products to clients with a solid knowledge of the component's life cycle within admissible ranges of operation. With that objective, industry spends millions of dollars every year in manufacturing, instrumenting and conducting validation tests. In order to reduce costs, manufacturers invest heavily in early stages of product design to reduce final project cost and development time. Decisions made in design phase have an impact of 70% of final cost. In that sense, numerical simulations have contributed to reduce the cost and time spent in product development through CAE applications in solid and fluid mechanics, and failure analysis play an important role in saving costs and ensuring safety.

The importance of reliable failure analysis motivates the development of trustworthy mathematical models and robust numerical methods. Several researchers have developed models of damage initiation, propagation and fatigue life of materials, using continuum damage models and fracture mechanics [1,2,3]. The *ad hoc* characteristics of those classical models prevent them to apply to a wider range of problems, affecting their predictability. Some of the limitations appear when dealing with crack initiation or branching, for example.

Recently, phase-fields have become a solid alternative to treat those difficulties in damage and fatigue modeling. Phase-field models were first developed to solve fluid separation problems [4]. Its capability of modeling sharp interfaces through a smooth continuous field extended its application to different multiphase problems with moving boundaries, including solidification [5], tumor growth [6], two-phase complex fluid flow [7] and fluid-structure interaction [8]. Over the last decade, phase-field models were used in simulations of brittle [9,10,11] and ductile fracture [12,13]. Phase-field damage models are able to capture many effects such as crack initiation, propagation, branching and coalescence. Crack branching is typically observed in dynamic fracture [14,15]. Fatigue effects were modeled using thermodynamically consistent approaches [16] and fractional derivatives [17]. Boldrini et al (2016) [18] developed a non-isothermal and thermodynamically consistent framework for damage and fatigue using phase-fields. Spatial convergence and 2D results were presented by Chiarelli et al (2017) [19]. A comparison between semi and fully implicit time integration schemes was analyzed by Haveroth et al (2018) [20].

Despite the ability to describe crack geometry and incorporate naturally fatiguing mechanisms and different constitutive laws, most examples of phase-field solutions studied so far include geometric characteristics that drive the crack path to determined places. The presence of notches, indentations, regions of stress concentration, is recurrent and leads to controlled experiments with a predictable crack path (always assuming a perfect material). In those models, there is no consideration of stochastic effects to account for material and manufacturing imperfection, surface roughness, or even misalignment of loading conditions that, in practice can drive failure to other locations.

Only a few works focused on studying stochastic nature of phase-field models. Uncertainty quantification and sensitivity analysis in the context of phase-field models for polymeric composites was addressed by Hamdia et al (2015) [21]. Authors used different methods to address the parametric sensitivity from a toughness test geometry with two notches. In that scenario, matrix elasticity modulus, volume fraction of clay platelets and the fracture energy of the matrix were the most influential parameters. In another application, sensitivity analysis was performed in a tumor growth phase-field model [22]. Using stochastic collocation, authors identified two most sensitive parameters: the rate of cellular mitosis and nutrient mobility. In that case, nutrient transport was governed by a traditional diffusion equation.

Besides the deterministic treatment of failure process, historically, phase-field models neglected nonlocal terms in the free energy potentials. The question of how those assumptions affect the model predictability of failure motivates a systematic way to evaluate model form uncertainty. Through determining the salient sources of uncertainty, educated modifications in the modeling process can be proposed, informed by the model itself. This self-assessment procedure could be further extended to incorporate stochasticity in space, and stochastic processes.

In this paper we develop a framework to assess model form uncertainty of a damage and fatigue phase-field model through uncertainty propagation and sensitivity. We define parameters related to damage and fatigue, as well as viscous damping effects, as random variables and solve a stochastic system of equations that model material damage using phase-fields. We compute the expected solution and standard deviation fields in univariate and multivariate setups. We define local sensitivity expectation, where we use complex-step differentiation [23] to compute local sensitivity at each collocation point in the random space. A variance-based method [24] is used to compute each parameter's Sobol indices in the global sensitivity analysis. These methods establish a framework to systematically investigate model form uncertainty. An incorrect operator can be detected by looking at the parameters that multiply them, which will be more sensitive and influential in the total output uncertainty. Assuming the model form is correct transfers the salient uncertainty associated with the operator to its parameters. We identify the parameters that most contribute to total output variance so that new models can be derived, mitigating model form uncertainty.

The paper is organized as follows. In Section 2 we present a stochastic version of the damage and fatigue phase-field model derived in Boldrini et al (2016) [18]. We discuss the system of PDEs, the finite element spatial discretization, the semi-implicit scheme for time integration and the stochastic discretization methods, namely Monte Carlo sampling and Probabilistic Collocation. Then, we present methods used for local and global sensitivity analysis in Section 3. In Section 4 we show the results of uncertainty and sensitivity for two representative numerical examples. Finally, we summarize and discuss the conclusions of the paper in Section 5.

2 | A STOCHASTIC DAMAGE AND FATIGUE PHASE-FIELD FRAMEWORK

We show a stochastic version of the phase-field framework for structural damage and fatigue presented in Boldrini et al (2016)[18], which consists in a deterministic system of coupled differential equations for the evolution of displacement $\mathbf{u}$, velocity $\mathbf{v} = \dot{\mathbf{u}}$, damage φ and fatigue $\mathcal{F}$. Damage φ is a phase-field variable describing the volumetric fraction of degraded material, taking values $\varphi = 0$ for virgin material, $\varphi = 1$ for fractured material, and can change between those states, $0 \leq \varphi \leq 1$, as a damaged material. The evolution equation for the damage field is an Allen-Cahn type, and is obtained along with the equations of motion for $\mathbf{u}$ and $\mathbf{v}$ through the principle of virtual power and entropy inequalities. The fatigue field $\mathcal{F}$ is treated as an internal variable, whose evolution equation is obtained through constitutive relations that must satisfy the entropy inequality for all admissible processes. The geometry is defined over a spatial domain $\Omega_d \subset \mathbb{R}^d$, $d = 1, 2, 3$ at time $t \in (0, T]$.

The overall construction of the model gives origin to a general set of equations that can take different forms based on suitable choices of free-energy potentials, boundary and initial conditions. The choice of free-energy potentials affects directly the final model form, the specific coupling between the fields of interest and material behavior. The free-energy potential $\mathcal{J}(\varphi, \mathcal{F})$, related to damage φ and fatigue $\mathcal{F}$ has the traditional form[18]

$$\mathcal{J}(\varphi, \mathcal{F}) = g_c \frac{\gamma}{2} |\nabla \varphi|^2 + \mathcal{K}(\varphi, \mathcal{F}), \tag{1}$$

where g_c is the Griffith energy, $\gamma > 0$ is the phase-field layer width parameter and $\mathcal{K}(\varphi, \mathcal{F})$ is a function that relates the change of damage to material fatigue. This general form for free-energy has been used since the first phase-field models, where the first term corresponds to *interfacial energy* and originates the Laplacian operator in Allen-Cahn type equations. The second term is called *mixing energy* in other disciplines, and may take different forms based on the application, even within damage models.

From the governing equations of the deterministic phase-field model we can identify many material parameters that are easily obtained from experimental procedures, namely elasticity constants (E and ν), and density ρ_0. For that reason, and to reduce the complexity of the analysis, we consider them to be deterministic. The remaining parameters, on the other hand, are either not physically measurable, or their value is uncertain, and are considered to be stochastic. First, we have those parameters which are proportionality constants due to mathematical modeling, such as rate of change of damage and fatigue, c and a, respectively. Similarly, phase-field layer width γ is a parameter that controls the diffusivity of damage field, therefore is a mathematical artifact that should be as close to zero as possible to recover the sharp interface. Furthermore, the viscous damping coefficient b is not promptly identifiable, and it would require a correlation with damping ratio to be obtained experimentally through modal testing. Finally, the Griffith energy g_c, although related to stress intensity factor, would require further experiments for each specific material, since its range varies broadly for materials with the same elastic properties.

We define the parameters mentioned as random variables and derive the stochastic version of the damage and fagitue phase-field model. Let $(\Omega_s, \mathcal{G}, \mathbb{P})$ be a complete probability space, where Ω_s is the space of outcomes ω, $\mathcal{G}$ is the $\sigma-$algebra and $\mathbb{P}$ is a probability measure, $\mathbb{P} : \mathcal{G} \to [0, 1]$. We define the five-dimensional set of random parameters $\xi(\omega) = \{\gamma(\omega), g_c(\omega), a(\omega), b(\omega), c(\omega)\}$. The random nature of ξ makes the operators and output fields to also be random. However, we simplify the notation and only explicitly represent the random parameters as $\xi = \xi(\omega)$, supressing the random variable indication elsewhere. Choosing appropriate free-energy potentials, we obtain the stochastic equations for a linear elastic and isotropic material without temperature evolution defined over $\Omega_d \times (0, T] \times \Omega_s$:

$$\begin{cases} \dot{\mathbf{u}} = \mathbf{v}, \\ \dot{\mathbf{v}} = \operatorname{div}\left((1-\varphi)^2 \frac{\mathcal{C}}{\rho_0}\mathbf{E}\right) + \frac{b(\omega)}{\rho_0}\operatorname{div}(\mathbf{D}) - \frac{\gamma(\omega)g_c(\omega)}{\rho_0}\operatorname{div}(\nabla\varphi \otimes \nabla\varphi) + \mathbf{f}, \\ \dot{\varphi} = \frac{\gamma(\omega)g_c(\omega)}{\lambda}\Delta\varphi + \frac{1}{\lambda}(1-\varphi)\mathbf{E}^T\mathcal{C}\mathbf{E} - \frac{1}{\lambda\gamma(\omega)}[g_c(\omega)\mathcal{H}'(\varphi) + \mathcal{F}\mathcal{H}'_f(\varphi)], \\ \dot{\mathcal{F}} = -\frac{\hat{F}}{\gamma(\omega)}\mathcal{H}_f(\varphi), \end{cases} \tag{2}$$

subjected to appropriate initial and boundary contitions, which depend on the physical problem. For the equation of motion, usually displacement or stress are known at the boundaries. For damage evolution, $\nabla\varphi \cdot \mathbf{n} = 0$ at the boundary, $\partial\Omega_d$.

The infinitesimal strain and the rate of strain tensors are represented by $\mathbf{E} = \nabla^S \mathbf{u}$ and $\mathbf{D} = \nabla^S \mathbf{v}$, respectively. $\mathcal{C}$ represents the elasticity tensor, as a function of Young's modulus E and Poisson coefficient ν. Parameter b is the viscous damping of the

material, ρ_0 corresponds to the material's density. Following an argument by Lemaitre and Desmorat (2005)[1], λ is constructed such that the rate of change of damage should increase as damage increases, following the relation:

$$\frac{1}{\lambda} = \frac{c(\omega)}{(1 + \delta - \varphi)^\varsigma},$$ (3)

where c and ς are positive parameters that should depend on the material. The relation includes δ, a small positive constant, in order to avoid numerical singularity.

The terms $\mathcal{H}'(\varphi)$ and $\mathcal{H}'_f(\varphi)$ are the derivatives of $\mathcal{H}(\varphi)$ and $\mathcal{H}_f(\varphi)$ with respect to φ and play an important role in the evolution of damage. Different choices for those potentials change the form of the transition of damage phase-field as fatigue changes from zero to g_c. Further details about the behavior of fatigue potentials can be found in Boldrini et al (2016)[18]. If we choose the transition to be continuous and monotonically increasing, suitable choices for the potentials are:

$$\mathcal{H}(\varphi) = \begin{cases} 0.5\varphi^2 & \text{for } 0 \le \varphi \le 1, \\ 0.5 + \delta(\varphi - 1) & \text{for } \varphi > 1, \\ -\delta\varphi & \text{for } \varphi < 0. \end{cases} \quad (4) \qquad \mathcal{H}_f(\varphi) = \begin{cases} -\varphi & \text{for } 0 \le \varphi \le 1, \\ -1 & \text{for } \varphi > 1, \\ 0 & \text{for } \varphi < 0. \end{cases} \quad (5)$$

The growth of the fatigue field $\mathcal{F}$ is controlled by the $\hat{F}$ parameter, which is related to the formation of micro-cracks that occur in cyclic loadings. Even in monotonic loadings there is growth of the fatigue variable, because a monotonic loading can be considered as one portion of a complete cyclic load. The form of $\hat{F}$ depends on the absolute value of the power related to stress in the virgin material:

$$\hat{F} = a(\omega)(1 - \varphi) \left| (C\mathbf{E} + b\mathbf{D}) : \mathbf{D} \right|,$$ (6)

where the parameter a in this case is chosen to give a linear dependence of the power of stress.

We construct a general framework to compute the stochastic solutions using three levels of discretization: in space, using finite element method; in time, using a semi-implicit integration scheme; and in the random space, where we choose our realizations randomly through Monte Carlo sampling, or by Probabilistic Collocation. Fundamentally, the finite element solver acts as a black box for any nonintrusive stochastic method.

2.1 | Spatial Discretization

We approximate a deterministic solution over its spatial domain Ω^d with finite element method, where the semi-discrete form of Equations (2) is obtained from the weak Galerkin form after multiplication by test functions and integration over the domain. A more detailed derivation of the spatial discretization in 2D can be found in Chiarelli et al (2017)[19]. Denoting $\dot{\hat{\mathbf{u}}} = \hat{\mathbf{v}}$ we write the semi-discrete form for an element k as

$$\begin{cases} \mathbf{M}^k \ddot{\hat{\mathbf{u}}}^k = \mathbf{K}_u^k \hat{\mathbf{u}}^k + \mathbf{K}_v^k \hat{\mathbf{v}}^k + \mathbf{w}_a^k + \mathbf{M}^k \hat{\mathbf{f}}^k, \\ \mathbf{M}_\varphi^k \dot{\hat{\boldsymbol{\varphi}}}^k = \left(\mathbf{P}_\varphi^k + \mathbf{K}_c^k \right) \hat{\boldsymbol{\varphi}}^k + \mathbf{w}_b^k + \mathbf{w}_c^k, \\ \mathbf{M}_\mathcal{F}^k \dot{\hat{\mathcal{F}}}^k = \mathbf{w}_d^k, \end{cases}$$ (7)

where $\mathbf{M}$, $\mathbf{M}_\varphi$ and $\mathbf{M}_\mathcal{F}$ are mass matrices related to displacement, damage and fatigue. In the equation of motion, $\mathbf{K}_u$ is the elasticity stiffness matrix degraded by damage, $\mathbf{K}_v$ is associated to viscous damping and $\mathbf{w}_a$ is a term related to gradient of damage that affects the displacement field. Term $\mathbf{P}_\varphi$ in the damage evolution equation includes the Laplacian and potential $\mathcal{H}'(\varphi)$. The influence of displacement in damage is represented by $\mathbf{K}_c$ and $\mathbf{w}_b$. Effect of potential $\mathcal{H}'_f(\varphi)$ is considered in term $\mathbf{w}_c$. $\mathbf{w}_d$ is the operator on the right-hand side of fatigue evolution equation. A detailed description of the finite element solution, interpolation, and derivative matrices, along with the complete definition of all operators is available in Appendix A.

We apply the standard assembly operation to obtain the global form of the operator matrices and we will drop the superscript k in the global sense.

2.2 | Time Discretization

We adopt a semi-implicit time integration scheme, where we solve each equation separately using a suitable implicit method, treating nonlinear terms and other variable fields explicitly. The methodology is based on the work by Haveroth et al (2018)[20],

where a detailed derivation can be found. We split the solution time interval $[0, T]$ in discrete time steps t_n with time increments given by $\Delta t = t_{n+1} - t_n > 0$, $n = 0, 1, \ldots$. We denote the global approximations for the variables at t_{n+1} as

$$\mathbf{u}_{n+1} = \hat{\mathbf{u}}(t_{n+1}), \quad (8) \qquad \mathbf{v}_{n+1} = \dot{\hat{\mathbf{u}}}(t_{n+1}), \quad (9) \qquad \boldsymbol{\varphi}_{n+1} = \hat{\boldsymbol{\varphi}}(t_{n+1}), \quad (10) \qquad \mathcal{F}_{n+1} = \hat{\mathcal{F}}(t_{n+1}). \quad (11)$$

We first discuss damage time integration. We use a backward Euler scheme to compute $\boldsymbol{\varphi}_{n+1}$ from Equation (7). Parameter λ, displacement and fatigue are treated explicitly using values from time step t_n. This simplifies the solution and avoids the use of iterative methods to treat the nonlinearity. Evolution of damage is then obtained by solving the linear system

$$\left[\mathbf{M}_\varphi - \Delta t\left(\mathbf{P}_\varphi + \mathbf{K}_c\right)\right]\boldsymbol{\varphi}_{n+1} = \mathbf{M}_\varphi\boldsymbol{\varphi}_n + \Delta t\left(\mathbf{w}_b + \mathbf{w}_c\right). \tag{12}$$

With the updated damage field, we use Newmark method to solve displacement and velocity in the equation of motion using the discrete form

$$\left[\alpha_1\mathbf{M} - \mathbf{K}_u - \alpha_4\mathbf{K}_v\right]\mathbf{u}_{n+1} = \mathbf{M}\left[\alpha_3\ddot{\mathbf{u}}_n + \alpha_2\dot{\mathbf{u}}_n + \alpha_1\mathbf{u}_n\right] + \mathbf{K}_v\left[\alpha_6\ddot{\mathbf{u}}_n + \alpha_5\dot{\mathbf{u}}_n - \alpha_4\mathbf{u}_n\right] + \mathbf{w}_a + \mathbf{M}\mathbf{f}_{n+1}. \tag{13}$$

with coefficients α_i, $i = 1, 2, \ldots, 6$. Definition of coefficients and further details on Newmark scheme can be found in Appendix B.

After the solution of Equation (13) we update the current acceleration and velocity fields using Equations (B31) and (B32), respectively. When imposing prescribed displacement $\bar{\mathbf{u}}(t_{n+1})$ we should also prescribe appropriate velocity and acceleration at the boundaries using

$$\ddot{\bar{\mathbf{u}}}_{n+1} = \frac{d^2}{dt^2}\bar{\mathbf{u}}(t_{n+1}) \quad \text{and} \quad \dot{\bar{\mathbf{u}}}_{n+1} = \frac{d}{dt}\bar{\mathbf{u}}(t_{n+1}), \tag{14-15}$$

where the bar symbol represents the prescribed degrees of freedom.

Finally, we update the fatigue variable using a Trapezoidal method given by

$$\mathcal{F}_{n+1} = \mathcal{F}_n + \frac{\Delta t}{2}\mathbf{M}_\mathcal{F}^{-1}\left[\mathbf{w}_d\left(\mathbf{u}_{n+1}, \mathbf{v}_{n+1}, \boldsymbol{\varphi}_{n+1}\right) + \mathbf{w}_d\left(\mathbf{u}_n, \mathbf{v}_n, \boldsymbol{\varphi}_n\right)\right]. \tag{16}$$

Algorithm 1 presents the final semi-implicit time integration scheme.

2.3 | Stochastic Discretization

Displacement, velocity, damage and fatigue from the phase-field framework solution are functions of random parameters; therefore, they are random fields. In order to obtain the statistical moments of those outputs we will solve the deterministic system of equations over an ensemble of different realizations, each of them with distinct parameter values. The inputs for each realization depends on the sampling method. In this work we employ Monte Carlo (MC) and Probabilistic Collocation Method (PCM). Since those methods are non-intrusive, the finite element solver acts as a black box, where the choice of parameter values and computation of statistical quantities are simply pre- and post-processing tasks, respectively.

2.3.1 | Probabilistic collocation method

The Probabilistic Collocation Method (PCM) poses a great advantage over the MC method, since PCM uses polynomial interpolation to approximate the solution in the random space. The mapping between the random and physical space is made through the probability density function of the uncertain parameters. Using orthogonal polynomials, such as Lagrange, the computation of expectation and variance reduces to running the simulation at the collocation points, reducing computational cost significantly, while improving convergence rates. In one dimension, the polynomial approximation of the solution $U_i(x, y, t; \xi)$ is given by:

$$\hat{U}(x, y, t; \xi) = \sum_{i=1}^{I} U(x, y, t; \xi_i)L_i(\xi), \tag{17}$$

where I is the number of realizations and $L_i(\xi)$ is the i-th Lagrange polynomial, with the orthogonality property, δ_{ij} being the Kronecker delta:

$$L_i(\xi_j) = \delta_{ij}. \tag{18}$$

Algorithm 1 Semi-implicit time integration scheme

1: **for** $n = 0 \rightarrow N - 1$ **do**
2:     Given $\mathbf{u}_n$, $\mathbf{v}_n$ and λ_n, solve Eq. (12) for $\boldsymbol{\varphi}_{n+1}$.
3:     Solve Eq. (13) for $\mathbf{u}_{n+1}$.
4:     Update acceleration $\mathbf{a}_{n+1}$ and velocity $\mathbf{v}_{n+1}$ using Eq. (B31) and (B32).
5:     Update the fatigue $\mathcal{F}_{n+1}$.
6:     Update the time step by adding the time increment Δt.
7: **end for**

Having approximated the solution in the random space, the expectation $\mathbb{E}$ in a one dimensional random space can be written as:

$$\mathbb{E}\left[U(x, y, t; \xi)\right] = \int_a^b \hat{U}(x, y, t; \xi)\rho(\xi)d\xi, \tag{19}$$

where $\rho(\xi)$ is the probability distribution function of ξ. In order to use Gauss quadrature, we must map the domains of the distribution to the interval $[-1, 1]$ in the standard domain of a variable η. The integral should then be written as:

$$\mathbb{E}\left[U(x, y, t; \xi)\right] = \int_{-1}^1 \hat{U}(x, y, t; \xi(\eta))\rho(\xi(\eta))J d\xi(\eta), \tag{20}$$

where $J = d\xi/d\eta$ represents the Jacobian of the transformation. To perform the integration, we must choose the number of integration points and find the points η_q and weights w_q for each integration point $q = 1, 2, \ldots, Q$.

Substituting Equation (17) in (20) we obtain

$$\mathbb{E}\left[U(x, y, t; \xi)\right] = \int_a^b \rho(\xi(\eta))J \sum_{i=1}^I U(x, y, t; \xi(\eta))L_i(\xi(\eta))d\xi(\eta)$$

$$\approx \sum_{q=1}^Q w_q \rho(\xi(\eta))J \sum_{i=1}^I U(x, y, t; \xi(\eta))L_i(\xi(\eta)). \tag{21}$$

Evaluating the realizations at the integration points q and using the orthogonality property of the Lagrange polynomials (18) the approximation (21) is simplified as a single summation in the collocation points:

$$\mathbb{E}\left[U(x, y, t; \xi)\right] = \sum_{q=1}^Q w_q \rho(\xi_q(\eta_q))JU(x, y, t; \xi_q(\eta_q)). \tag{22}$$

We use a linear affine mapping from the standard to the real domain: $\xi_q(\eta_q) = a + \frac{(b-a)}{2}(\eta_q + 1)$. This mapping gives us the Jacobian (for a one-dimensional integration) simply as $J = (b - a)/2$. In practice, after we find the quadrature points in the standard domain, we use the mapping to find the respective values of the random variable in our interval.

We can now approximate the integral and rewrite it as a summation over the collocation points, again assuming a *uniform distribution* for the parameters over the interval $[a, b]$, which gives us a constant value of $\rho(\xi) = 1/(b - a)$. The expectation becomes $\mathbb{E}[U(x, y, t; \xi)] = \frac{1}{2}\sum_{q=1}^Q w_q U(x, y, t; \xi_q)$. Similarly to the Monte Carlo method, the standard deviation is $\sigma[U(x, y, t; \xi)] = \sqrt{\frac{1}{2}\sum_{q=1}^Q w_q \left(U(x, y, t; \xi_q) - \mathbb{E}[U(x, y, t; \xi)]\right)^2}$.

If we want to generalize PCM for higher dimensions, it is just a matter of having additional integrals to Equation (19). In discrete form, this reduces to

$$\mathbb{E}\left[U(x, y, t; \xi^1, \ldots, \xi^k)\right] = \mathbb{E}_{PCM}\left[U(x, y, t; \xi^1, \ldots, \xi^k)\right]$$

$$\approx \sum_{q=1}^Q \cdots \sum_{l=1}^L w_q \ldots w_l \rho(\xi_q) \ldots \rho(\xi_l) J_q \ldots J_l U(x, y, t; \xi_q^1, \ldots, \xi_l^k) \tag{23}$$

where we have k summations, one for each dimension in the random space. In ξ_l^k the superscript indicates the dimension in the random space, and the subscript specifies the collocation point in that dimension. Simplifying the notation using $\mathbb{E}\left[U(x, y, t; \xi^1, \ldots, \xi^k)\right] = \mathbb{E}[U]$, the standard deviation becomes

$$\sigma\left[U(x, y, t; \xi^1, \ldots, \xi^k)\right] = \sigma_{PCM}\left[U(x, y, t; \xi^1, \ldots, \xi^k)\right]$$

$$\approx \sqrt{\sum_{q=1}^{Q} \cdots \sum_{l=1}^{L} w_q \ldots w_l\, \rho(\xi_q) \ldots \rho(\xi_l)\, J_q \ldots J_l\, \left(U(x, y, t; \xi_q^1, \ldots, \xi_l^k) - \mathbb{E}[U]\right)^2}. \tag{24}$$

Here, we are required to perform a tensor product to obtain the set of parameters for each realization. On one side, we have the flexibility to introduce anisotropy on the sample space by using different number of integration points in each dimension, depending on the parameter. Moreover, once we have simulated all multidimensional tensor product simulations, obtaining first and total-order sensitivity indices is just a matter of post-processing. On the other hand, if we want to have accurate results in higher dimensions (more than the 5 dimensions considered here) the tensor product increases the number of simulations exponentially. In that case, we could use Smolyak sparse grids to reduce the number of realizations[25]. In all examples showed in this work we assume the random variables to be mutually independent. That assumption may not always hold true for a specific scenario, in which case a proper treatment should be given due to correlation between parameters.

3 | SENSITIVITY ANALYSIS

The stochastic methods presented give us the ability to propagate parametric uncertainty through the model and obtain statistical information from the solution. We can take a step further and use the stochastic information to systematically study the importance of each parameter to solution uncertainty. Using a univariate PCM framework we can compute local sensitivity in a probabilistic way. Through multivariate PCM uncertainty propagation we can analyze the influence of each parameter in the total variance, by calculating sensitivity indices. In this Section, we derive the local and global sensitivity frameworks from the phase-field model stochastic discretization.

3.1 | Stochastic Sensitivity Analysis

In local sensitivity analysis, we study the effect of only one parameter while keeping all others at their expected values. The sensitivity of the output $U(\xi^j)$ with respect to input parameter ξ^j, $j = 1, 2, 3, 4, 5$ being one of the parameters in $\xi(\omega) = \{\gamma(\omega), g_c(\omega), a(\omega), b(\omega), c(\omega)\}$, is also a random variable, so we compute its expected value as

$$\overline{S}_{U,\xi^j} = N_f \mathbb{E}(S_{U,\xi^j}) \tag{25}$$

where N_f is a normalization factor defined as

$$N_f = \frac{\bar{\xi}^j}{\bar{U}} \tag{26}$$

In Equation (26), $\bar{\xi}^j$ is the expected value of the input parameter under consideration and $\bar{U}$ is the volume average of the expected solution U. In Equation (25) we consider the expectation of sensitivities over all the parameter intervals, computed using PCM as

$$\mathbb{E}\left[(S_{U,\xi^j})\right] \approx \frac{1}{2} \sum_{q=1}^{Q} w_q S_{U_q,\xi_q^j} \tag{27}$$

with S_{U_q,ξ_q^j} being the sensitivity at collocation point q for parameter j. The sensitivity around each integration point is computed using complex-step differentiation[23]. Unlike traditional finite-difference approximations, in complex-step differentiation we perturb the imaginary part of the parameter. Let $\xi^j = p + ih$ and $h \in \mathbb{R}$. Expanding $U(\xi)$ in Taylor series about the real part p we obtain

$$U(\xi^j) = U(p + ih) = U(p) + ihU'(p) - h^2 U''(p) + \mathcal{O}(h^2). \tag{28}$$

We then take the imaginary part on both sides to obtain the derivative of U around the real part of ξ:

$$U'(p) = S_{U,\xi^j} \approx \frac{Im(U(p+ih))}{h} \tag{29}$$

We can also take the real part of $U(p + ih)$ to recover the unperturbed solution and compute the expectation used in the normalization factor, Equation (26).

The complex-step differentiation is second-order accurate and allows for small perturbations without incurring round-off and cancellation errors. Using complex-step differentiation has another enormous advantage over finite-difference schemes. We only need to evaluate one solution at each point, instead of two. We take the imaginary part of the solution to compute the derivative, and use the real part to calculate the volume average of the expected solution in Equation (26).

Remark 1. Using MATLAB, this method can be applied almost immediatly by running the simulation with an imaginary perturbation. However, in the derivation of complex-step differentiation, we have to assume that $U(\xi)$ is analytic, implying the Cauchy-Riemman equations must hold. We must also assure all operators in the implementations to be analytic [23] . Most of operators in MATLAB are compatible with complex numbers. Operations like maximum, minimum, greater or less than, should always compare only the real part. Moreover, when transposing vectors and matrices, we should use the dot-apostrophe transpose, that do not take conjugate of the elements. The only operation that we must redefine to be analytic is the absolute value, implemented as

$$\text{abs}(x + iy) = \begin{cases} -x - iy, & \text{if } x < 0 \\ +x + iy, & \text{if } x \geq 0 \end{cases} \tag{30}$$

3.2 | Global sensitivity analysis

In a global analysis we are interested in how sensitive is the output when we perturb all input parameters. We use a variance-based method based on Sobol indices [26], where we compute the relative importance of input parameters to total output variance. To derive the algorithms for variance-based sensitivity analysis we refer to Saltelli et al (2010) [24]. For simplicity, we now denote our solution vector only as $U(\xi) = f(\xi^1, \xi^2, \ldots, \xi^k)$, a random variable function of random parameters ξ^j, $j = 1, 2, \ldots, k$, k being the total dimension of the random space (the number of random parameters). The effect of parameter ξ^j on variance V is

$$V_{\xi^j}\left(\mathbb{E}_{\boldsymbol{\xi}^{\sim j}}(U|\xi^j)\right) \tag{31}$$

where $\boldsymbol{\xi}^{\sim j}$ denotes the combination of all possible values for random parameters with the exception of ξ^j, which is fixed at some value. We interpret Equation (31) as taking the expected value of U having fixed a value for ξ^j, and then taking the variance over all possible values of ξ^j. From the Law of Total Variance, we have

$$V_{\xi^j}\left(\mathbb{E}_{\boldsymbol{\xi}^{\sim j}}(U|\xi^j)\right) + \mathbb{E}_{\xi^j}\left(V_{\boldsymbol{\xi}^{\sim j}}(U|\xi^j)\right) = V(U) \tag{32}$$

The second term on the left-hand side is called the residual and $V(U)$ is the total variance. Normalizing Equation (32) we obtain the sensitivity index that measures the effect on total variance by random variable ξ^j as:

$$S^j = \frac{V_{\xi^j}\left(\mathbb{E}_{\boldsymbol{\xi}^{\sim j}}(U|\xi^j)\right)}{V(U)} \tag{33}$$

The sensitivity indices S^j only measure the first-order effect on variance from ξ^j, and disregards the interactions between ξ^j and other parameters. The total sum of S^j should be less than 1, the remainder being the high-order interactions between the parameters.

If we would like to compute any second, third, or higher-order indices, we would have to repeat this procedure for all combinations of interactions. An alternative is to compute the sensitivity index related to a given parameter and all its possible interactions with all parameters. In order to obtain the total effect index S_T^j we start from the total normalized variance and subtract the contribution of all first and high-order effects that do not include ξ^j. We write

$$S_T^j = 1 - \frac{V_{\boldsymbol{\xi}^{\sim j}}\left(\mathbb{E}_{\xi^j}(U|\boldsymbol{\xi}^{\sim j})\right)}{V(U)} \tag{34}$$

In practical terms, for every combination of parameters that do not include ξ^j we compute the expectation with respect to ξ^j. That means performing different combinations of univariate expected solutions with respect to ξ^j. Then, all these different

---

Algorithm 2 Stochastic Sensitivity Analysis

1: **for** Random parameters $\xi^j = 1 \rightarrow k$ **do**
2:    Choose a perturbation h, and define the random parameter as $U(\xi^j) = U(p + ih)$.
3:    Solve the stochastic problem in one dimension with perturbed inputs $\xi^j = p + ih$.
4:    Compute the sensitivity of the solution at every collocation point following Eq. (29).
5:    Compute the expectation of sensitivities $\mathbb{E}\left[(S_{U,\xi^j})\right]$, following Eq. (27).
6:    Compute the normalization factor N_f using the volume average of expected solution, Eq. (26).
7:    Given $\mathbb{E}\left[(S_{U,\xi^j})\right]$ and N_f compute the local sensitivity $\overline{S}_{U,\xi^j}$ using Eq. (25).
8: **end for**

Algorithm 3 Global Sensitivity Analysis

1: For all k random parameters, solve the $k-$dimensional stochastic problem employing PCM.
2: **for** Random parameters $\xi^j = 1 \rightarrow k$ **do**
3:    Given the tensor product results in all collocation points, compute first-order sensitivity index S^j using Eq. (33).
4:    Given the tensor product results in all collocation points, compute total-order sensitivity index S_T^j using Eq. (34).
5: **end for**

---

expectations compose a $k - 1$ dimensional random space, from which we compute the variance. From 5-D PCM full tensor product we already possess all possible combinations between the parameters, so the computation of S^j and S_T^j are just a matter of postprocessing the realizations.

3.3 │ Integrated Sensitivity-Uncertainty Quantification Framework

Given the stochastic discretization methods from Section 2.3 as integrating building blocks, we formulate a framework to quantify model-form uncertainty through a parametric uncertainty/sensitivity propagation. The stochastic and global sensitivity analyses are naturally integrated to the framework using PCM. The stochastic sensitivity procedure is summarized in Algorithm 2, where the solution sensitivity with respect to a given parameter is obtained through the complex-step differentiation. The participation of each parameter in total uncertainty given by sensitivity indices is outlined in Algorithm 3. We further elaborate on the integrated framework's development and capabilities via two canonical examples in the next Section.

4 │ NUMERICAL RESULTS

We now present two representative numerical examples to show the capabilities of the proposed methodology to assess uncertainty and sensitivity of damage phase-field models. The first example is the single-edge notched tensile test case, a traditional benchmark test with mode I crack propagation. With the notched geometry, we first investigate the convergence of MC and PCM methods in the univariate and multivariate uncertainty propagation. Then, we show the expectation and standard deviation of damage evolution for each parameter and compare that with 5-D parametric uncertainty propagation. Next, we show local sensitivity expectation results for each parameter in the univariate framework. Last, we compute Sobol indices in the global sensitivity analysis and comment on the different influence of each parameter.

The second example is a standard tensile test specimen, symmetric and with no notches or existing cracks. We run the stochastic framework and show the expected crack path and its uncertainty. We also run local and global sensitivity analyzes to understand how the lack of pre-existing crack or notch affects the output uncertainty.

4.1 │ Single-Edge Notched Tensile Test

The notched geometry is a benchmark test, consisting in a square of material with a pre-existing crack in the middle of the specimen, see Figure 1. We constrain the body at the top and apply a prescribed displacement at the bottom, at a rate of $3 \times 10^{-3} \; m/s$. The finite element mesh has 3395 nodes, composing 6498 linear triangle elements with smallest element size being

TABLE 1 Expected value of stochastic parameters for single-edge notched tensile test.

Parameter	Value
a (rate of change of fatigue)	$5 \times 10^{-7}\ m^2$
b (viscous damping)	$1 \times 10^{8}\ N s/m^2$
c (rate of change of damage)	$1 \times 10^{-5}\ m/N s$
g_c (Griffith energy)	$2700\ N/m$
γ (phase-field layer width)	$1 \times 10^{-3}\ m$
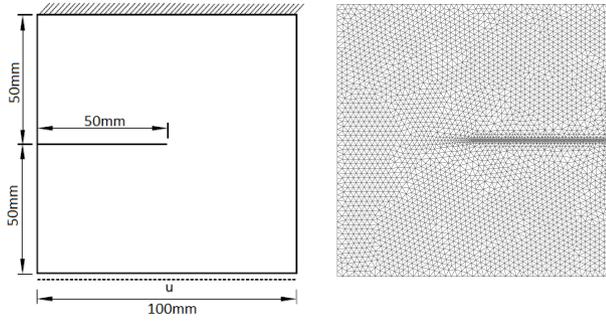
FIGURE 1 Left: Geometry and boundary conditions for single-edge notched tensile test. Right: Finite element mesh.
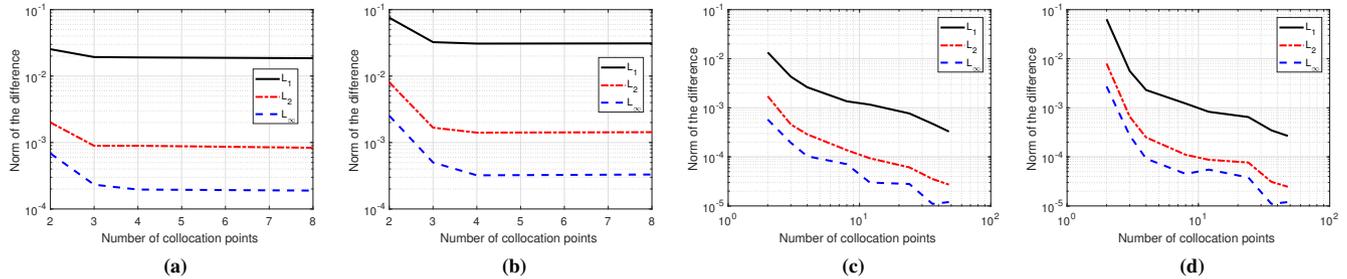
FIGURE 2 Univariate simulations: expectation (a) and standard deviation (b) error between MC results with 10^4 samples and solutions from PCM with different number of collocation points. We observe that with 4 points we obtain comparable accuracy in PCM. Expectation (c) and standard deviation (d) PCM convergence, where the reference for error computation is a solution with 100 collocation points in the univariate case. The convergence rate is close to linear.

0.404 mm. The final time is $T = 0.5\ s$ and we integrate the solution over time-steps of $\Delta t = 1 \times 10^{-3}\ s$. We consider a material with $E = 160\ GPa$, $\nu = 0.3$ and $\rho_0 = 7800\ kg/m^3$ under plane stress conditions with thickness of $h = 5\ mm$. As stated in Section 2.3, we assume a uniform distribution for the random variables, with a range of $\pm 10\%$ from their expected values, which are given in Tables 1.

4.1.1 | Convergence

We compare MC and PCM solutions at final time, and compute the error between them under L_1, L_2 and L_∞ norms for different number of PCM collocation points in Figure 2(a) and (b). Moreover, we investigate the convergence of PCM using a 100-point solution as reference, since we do not know the exact solution, and plot the results in Figure 2(c) and (d). For all univariate convergence analysis we consider γ as the random parameter.

Figure 3(a) and (b) show the error between MC and PCM in the multivariate case, considering the parameters from Table 1, thus defining a 5-D random space. Again, we compare the error between expectation and standard deviation of 10^4 MC realizations and PCM with different number of collocation points. On Figure 3(c) and (d), we see the convergence of PCM in 5 dimensions, where we use a solution with 6 points in each dimension as reference (of total 6^5 PCM points). The plots on Figure show a slope of 5 for expectation and 6 for standard deviation, an increased convergence rate when compared to the univariate case.

4.1.2 | Uncertainty and sensitivity analyses

We first investigate the univariate uncertainty propagation, where we assume that each random parameter has a uniform distribution centered at the values on Table 1 with 10% variation to left and right. In this 1-D parametric setting, we assume that the other parameters are deterministically known at their expected values. Figure 4 shows the damage field expectation and standard deviation when we consider the phase-field layer width γ as uncertain, while keeping the other parameters fixed in PCM simulations with 4 integration points. The expected crack propagates to the right, as we could expect from a tensile load, and the uncertainty follows the crack tip. In Figure 5 we plot the damage field from random γ over the crack propagation line (at $y = 50\ mm$, from $50\ mm \leq x \leq 100\ mm$). Looking at the damage field profiles from the expected solution we see the crack tip

(a)   **(b)**   **(c)**   **(d)**
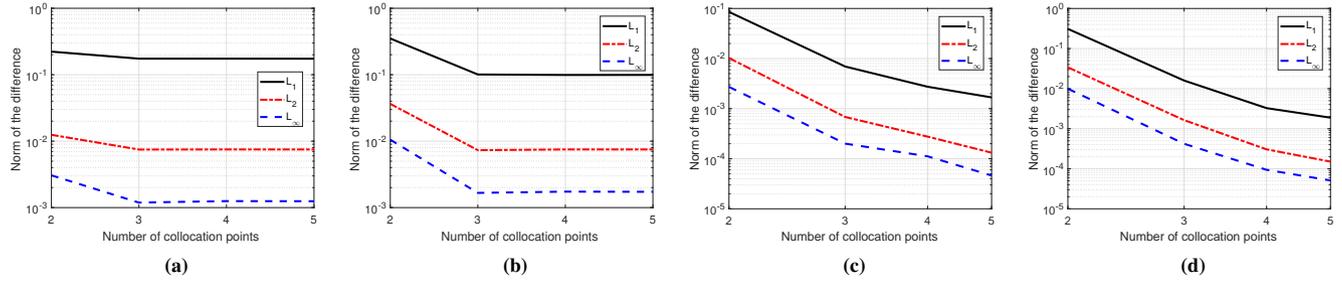
FIGURE 3 (a) and (b): Comparison between MC results with 10^4 samples, and solutions from PCM with different number of points in each dimension in the multivariate case. With higher dimensions the advantage of PCM over MC becomes more evident, with only 3 points needed in each dimension to stabilize the error in both expectation (a) and standard deviation (b). (c) and (d): Convergence of damage field on multivariate PCM simulations of notched geometry, where the reference for error computation is a solution with 6 collocation points in each dimension. We obtain slope 3.3 for expectation (c) and 3.14 for standard deviation (d).

(a) Time $t = 0.3\ s$.   **(b)** Time $t = 0.4\ s$.   **(c)** Time $t = 0.5\ s$.

(d) Time $t = 0.3\ s$.   **(e)** Time $t = 0.4\ s$.   **(f)** Time $t = 0.5\ s$.
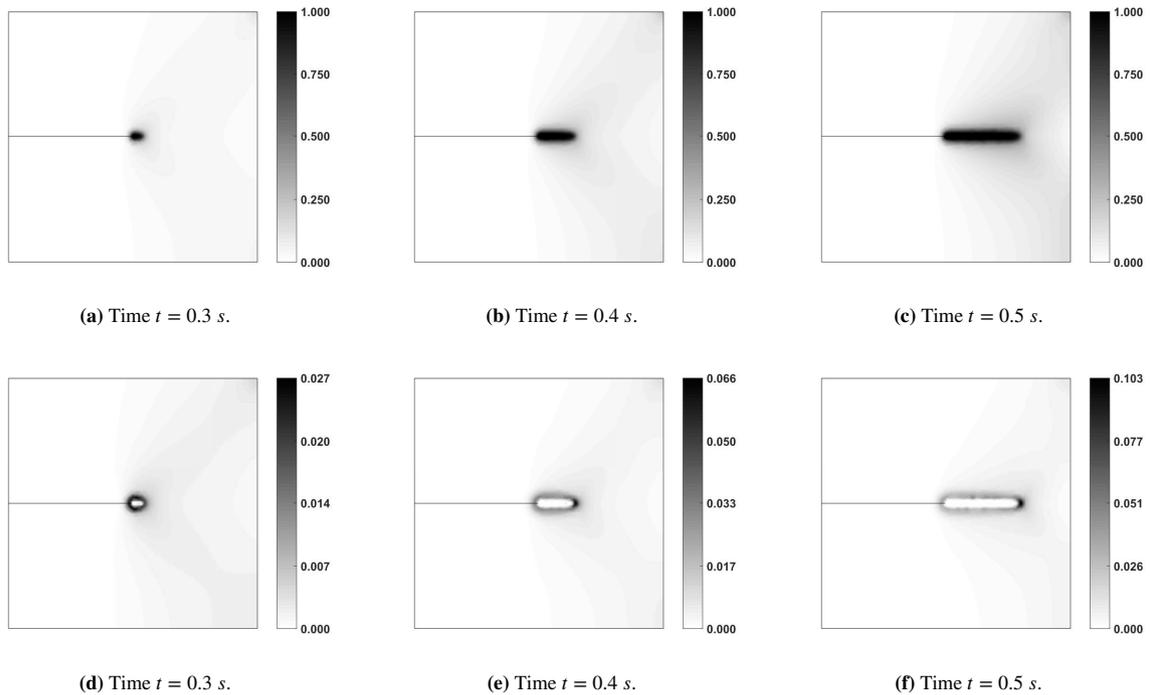
FIGURE 4 Damage phase-field expectation (top) and standard deviation (bottom) after crack propagation taking γ as random input. From tensile load the crack propagates in Mode-I as expected. γ has influence around the crack path, because it controls the diffusion of damage. Once the crack propagates and the expected value is 1 in the crack path, the uncertainty vanishes in the cracked region. However, the deviation around the crack tip grows with time.

as a moving interface. The standard deviation's peak follows the interface and grows in time. Since γ controls the diffusivity we see that with increasing uncertainty the interface profile of the expected solution becomes less sharp with time.

For the other parameters, the damage field expectation is similar to the ones shown in Figure 4. The major difference lies in the deviation field, as shown in Figure 6, where we see that for the other variables the uncertainty is more concentrated around the crack tip. This example has a known crack path, so most of uncertainty is related to the speed of crack growth through the Griffith fracture energy g_c that controls how fast damage grows with intermediate values of fatigue, and the rate of change of damage c, directly affecting damage time evolution.

Still in the univariate framework, we use complex-step differentiation to evaluate the stochastic sensitivity of every random parameter, where the perturbation is chosen to be $h = 0.001(\xi^j_{max} - \xi^j_{min})$. Figure 7 shows expectation of damage sensitivity fields at final time $T = 0.5\ s$. We make two observations here. First, the sensitivity fields show that damage increases at the crack tip when we increase γ, a and c. By increasing b we damp vibrations, thus, reducing damage. Again, the effect of g_c is visible, where increasing its value we require higher levels of fatigue to drive damage towards 1, thus the sensitivity around the crack tip is negative. Second, if we order sensitivity and standard deviation by their maximum absolute values, we obtain the

(a) Damage expectation profile.

(b) Damage standard deviation profile.
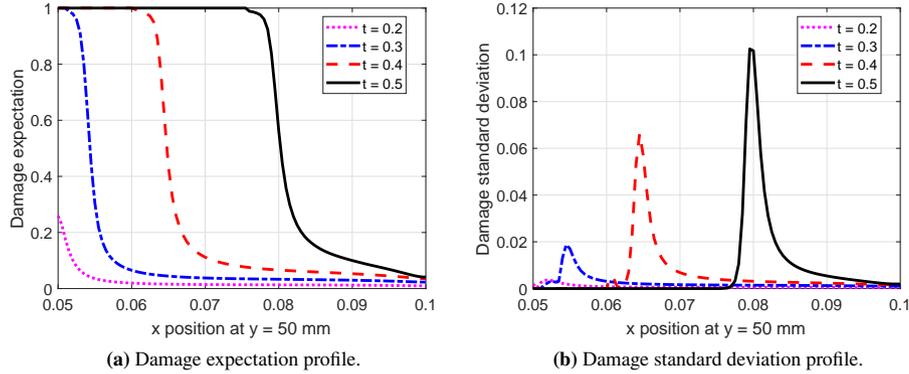
FIGURE 5 Time evolution of damage phase-field expectation and standard deviation profiles at the crack path line taking γ as random input. From damage expectation we observe the crack tip as a moving interface. The standard deviation peak follows the advecting boundary and grows in time, which makes the expected interface less sharp.

(a) Rate of change of fatigue a.

(b) Viscous damping b.

(c) Rate of change of damage c.

(d) Griffith fracture energy g_c.
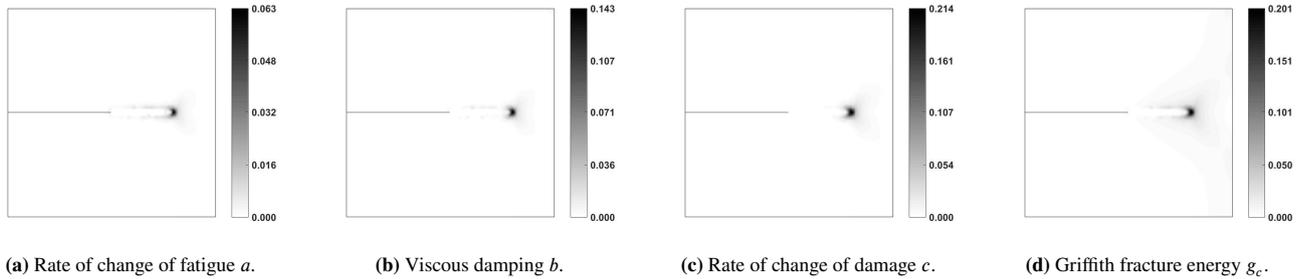
FIGURE 6 Damage phase-field standard deviation after crack propagation in univariate uncertainty quantification. Fatigue parameter a and viscous damping b do not propagate uncertainty as much as Griffith energy g_c and rate of change of damage parameter c. Since the crack path is defined by geometry, the majority of uncertainty is related to the speed of crack propagation, controlled mostly by g_c and c.

same decreasing order for both: c, g_c, b, γ, a, with similar proportionality between them in the two cases. Both results evidence that with a clear crack location and path, speed of propagation drives uncertainty and sensitivity.

From the univariate uncertainty propagation and the stochastic sensitivity analysis, we identify the most influential parameters when we assume all others to be known. Now we show results of a 5-D PCM simulation, where we consider all parameter combinations through tensor product, using 6 points in each dimension. Figure 8 shows the evolution of damage phase-field profiles at the crack path over time. The maximum standard deviation at final time (0.257) is comparable to peak uncertainty of g_c (0.201) and c (0.214).

In order to quantify the relative participation of each parameter in 5-D uncertainty, we compute the Sobol indices S^j and S^j_T from Eq. (33) and (34), respectively. Figure 9 shows the total deviation field, as a reference, and sensitivity index fields S^j at final time for all parameters. Despite γ having high maximum value of its sensitivity index, we point out that most of its influence is around the crack, where the uncertainty is small. Ahead of the crack, γ has no influence in uncertainty in this case where the path is defined. We see again that at the region of high uncertainty g_c and c play an important role when we only consider their sole effects. We plot the total sensitivity index fields S^j_T in Figure 10. We see that high order interactions between the parameters have great impact over the sensitivity indices. In the majority of the geometry, the fields are uniform with base value around 0.4, except for γ. The influence of g_c and c is carried over the other parameters in the region ahead of the crack, with g_c still being the parameter that has most impact ahead of the crack.

From single-edge notched tensile test uncertainty and sensitivity analyses it is clear that the load conditions and geometric singularity define the position of crack initiation and its path. Parameters that control rate of change of damage, such as g_c or c, are more sensitive and contribute more to solution uncertainty. For general geometries and load situations, we may expect a shift in the relative contribution of total uncertainty. Take the sensitivity indices from Figure 9, for example. Uncertainty that is not around the crack tip in the direction of crack propagation is dominated almost entirely by γ and g_c. In cases where the uncertainty is not concentrated around a specific region of the geometry, we can expect γ and g_c to have stronger influence. Not

(a) Phase-field layer width γ.

(b) Griffith fracture energy g_c.

(c) Rate of change of fatigue a.

(d) Viscous damping b.

(e) Rate of change of damage c.
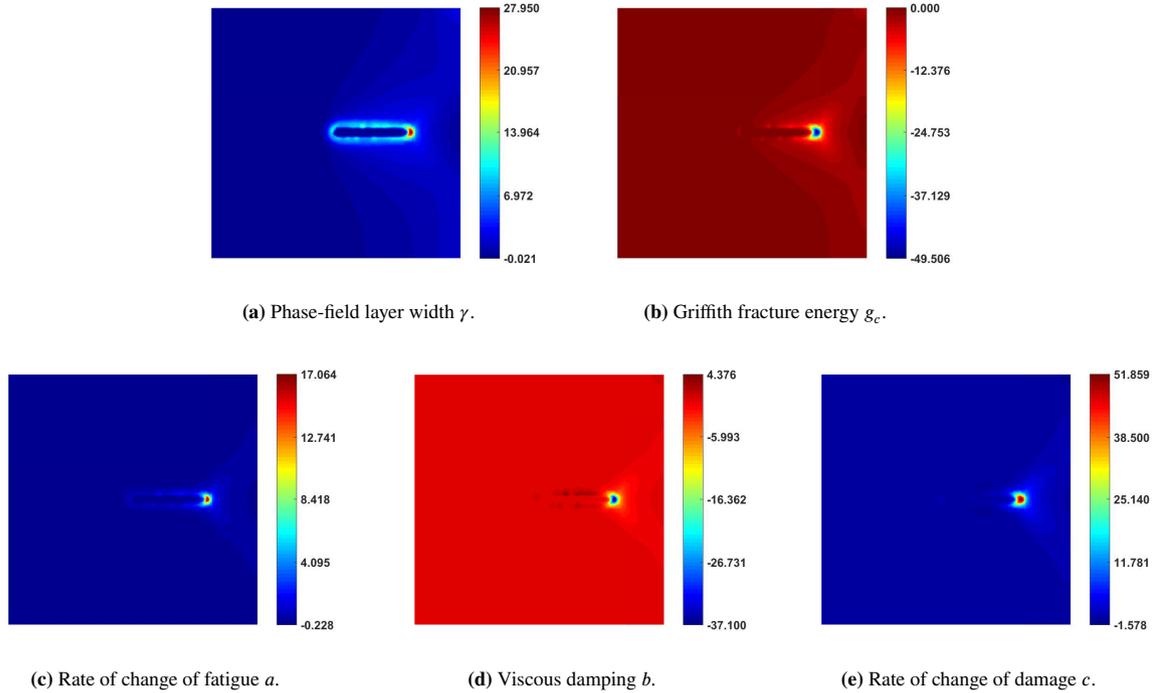
FIGURE 7 Expected sensitivity fields with respect to each input parameter. Similarly to standard deviation fields, local sensitivity results also point to c and g_c, related to propagation speed, as parameters with more sensitive output, since we have a specific crack initiation location and path.

(a) Damage expectation profile.

(b) Damage standard deviation profile.
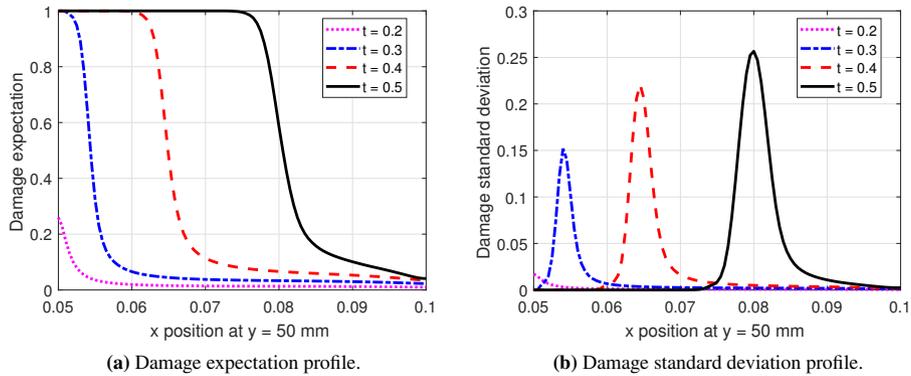
FIGURE 8 Time evolution of damage phase-field expectation and standard deviation profiles at the crack path line when propagating the uncertainty of all 5 random parameters. We observe that the combined effect of all parameters results in a larger standard deviation around the crack tip at final time, comparable to peak values of c and g_c uncertainties.

surprisingly, both parameters are multiplying the Laplacian in damage equation, which arises from the squared gradient, a local interaction term in the free-energy potential.

4.2 | Tensile Test Specimen

The tensile test geometry without notch from Figure 11 is the standard design with a mesh of 3912 nodes and 7236 linear triangle elements, where we also constrain one of its ends and apply a prescribed displacement of $1.5 \times 10^{-3} \ m/s$ until $T = 0.5 \ s$, with time increments of $\Delta t = 5 \times 10^{-4} \ s$. The smallest element size in the mesh is $0.614 \ mm$. We consider the same material properties and thickness from the notched case, with expected values for the stochastic parameters shown on Table 2.

We investigate the multivariate uncertainty propagation in the tensile test case. Figure 12 shows the convergence of 5D PCM using the solution of 6 points in each dimension as a reference. Due to the absence of an initial crack, the convergence of the

(a) Total deviation field.

(b) Phase-field layer width γ.

(c) Griffith fracture energy g_c.

(d) Rate of change of fatigue a.

(e) Viscous damping b.

(f) Rate of change of damage c.
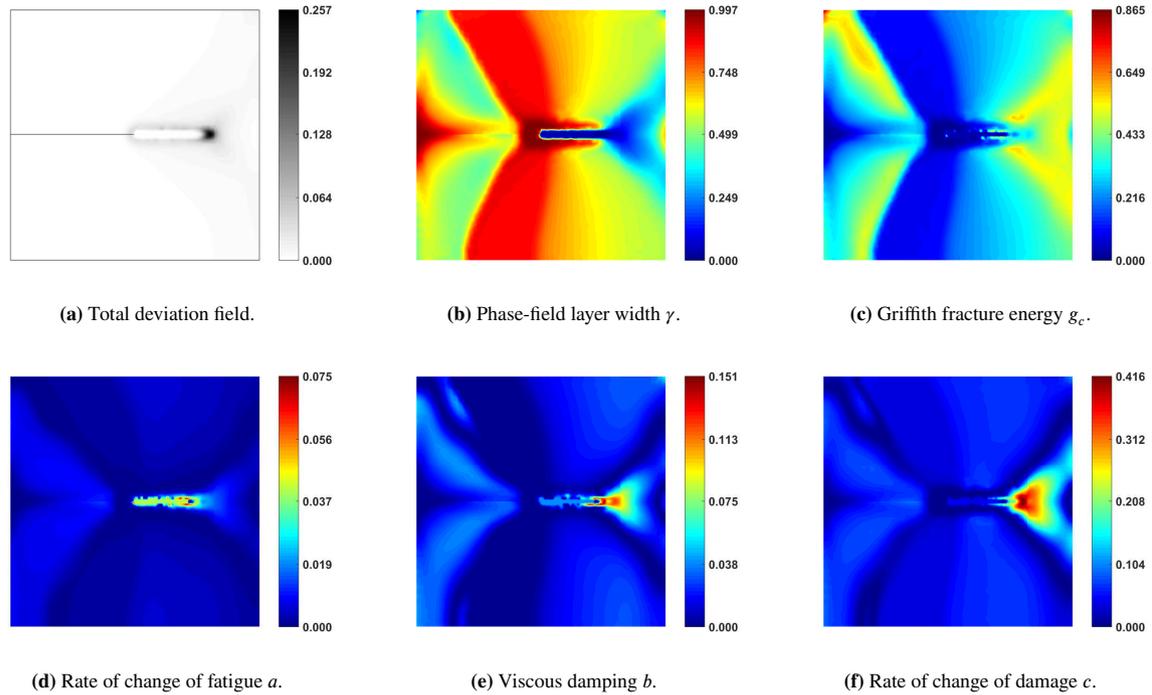
FIGURE 9 Notched tensile total damage deviation field and sensitivity indices (S^j) fields for all parameters using 6 points in each dimension at final time $T = 0.5\ s$. Ahead of the crack, g_c and c are the most influential parameters to total damage field variance. The remaining parameters have little participation at the most uncertain region of the geometry.

(a) Total deviation field.

(b) Phase-field layer width γ.

(c) Griffith fracture energy g_c.

(d) Rate of change of fatigue a.

(e) Viscous damping b.

(f) Rate of change of damage c.
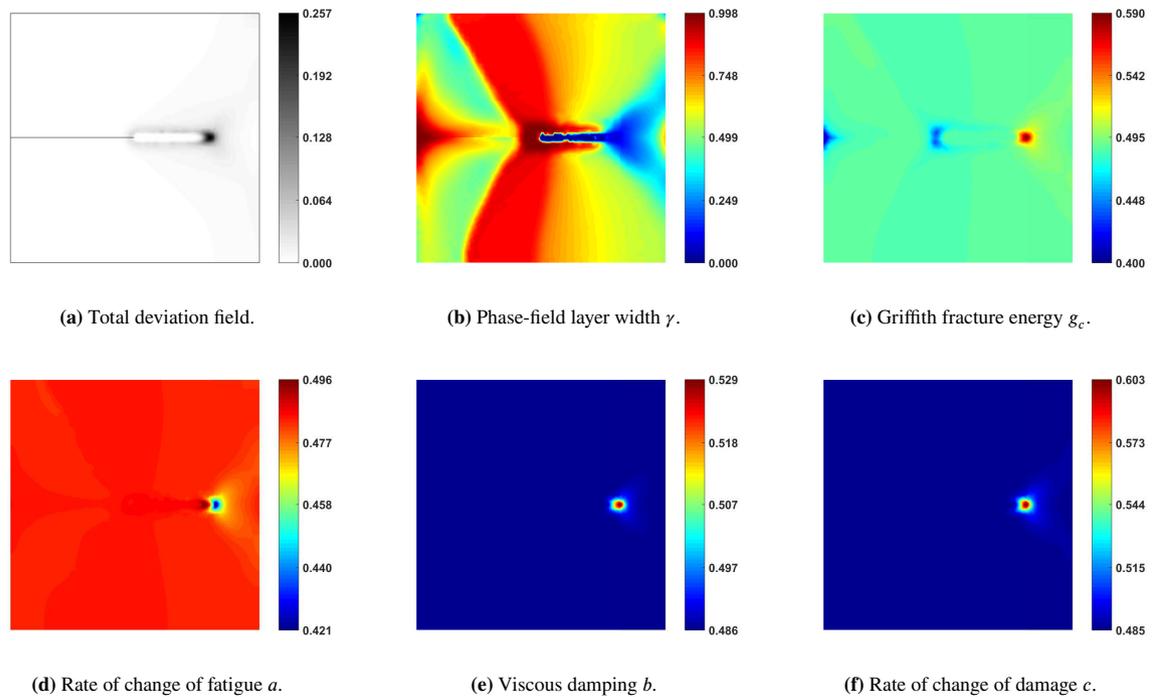
FIGURE 10 Notched tensile total damage deviation field and total effect sensitivity indices (S_T^j) fields for all parameters using 6 points in each dimension at final time $T = 0.5\ s$. When we combine parameter effects and include their interactions the dominant sensitivity at the crack tip gets carried out to all parameter indices. In the remaining regions, the sensitivity index is uniform except for γ: the diffusion coefficient is more influential throughout the specimen.

expected solution and deviation has a lower rate when compared to the single-edge notched test. Figures 13 and 14 show the expectation and standard deviation of the damage field when we consider 5-dimensional PCM simulations with 6 integration
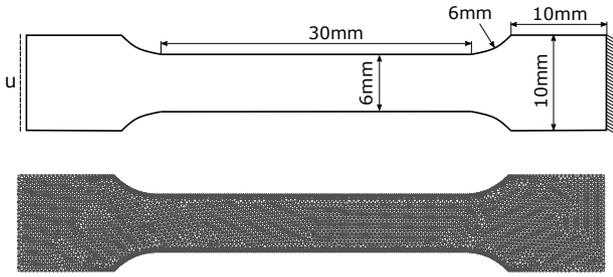
FIGURE 11 Top: Geometry and boundary conditions for tensile test specimen. Bottom: finite element mesh.

TABLE 2 Expected value of stochastic parameters for tensile test specimen.

Parameter	Value
a (rate of change of fatigue)	$5 \times 10^{-7} \; m^2$
b (viscous damping)	$1 \times 10^8 \; Ns/m^2$
c (rate of change of damage)	$2 \times 10^{-6} \; m/Ns$
g_c (Griffith energy)	$2700 \; N/m$
γ (phase-field layer width)	$3 \times 10^{-4} \; m$

(a) Expectation.

(b) Standard deviation.
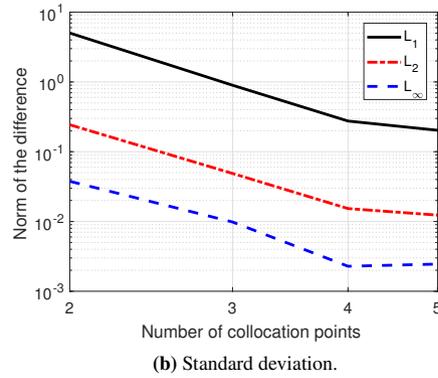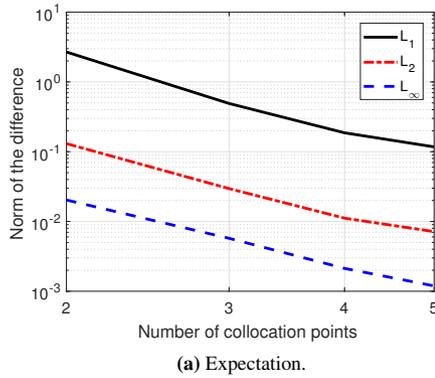
FIGURE 12 Convergence of damage field in multivariate PCM simulations for tensile test specimen, where the reference for error computation is a solution with 6 collocation points in each dimension. We have lower convergence rates when compared to notched geometry due to due to more uncertainty of crack location.

(a) $t = 0.46 \; s$.

(b) $t = 0.48 \; s$.

(c) $t = 0.5 \; s$.
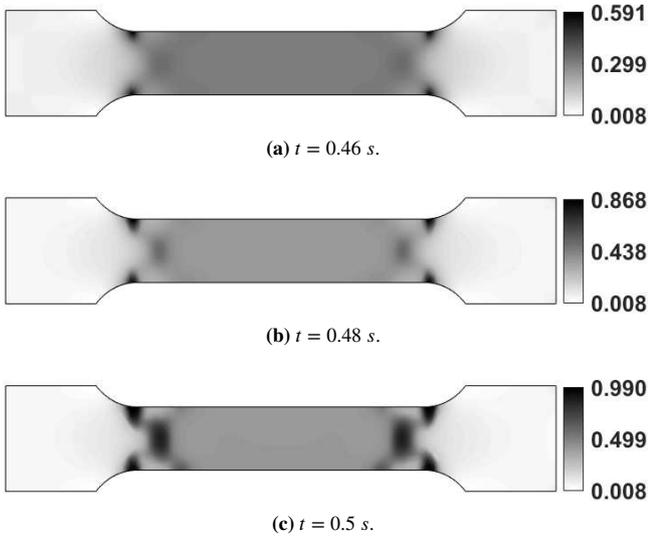
FIGURE 13 Damage phase-field expectation taking all parameters in ξ as random inputs. From tensile load we see the appearance of 4 possible crack initiation points, based on the stress concentration profile from the geometry. The expected solution at final time gives a curved crack path at both sides of the geometry.
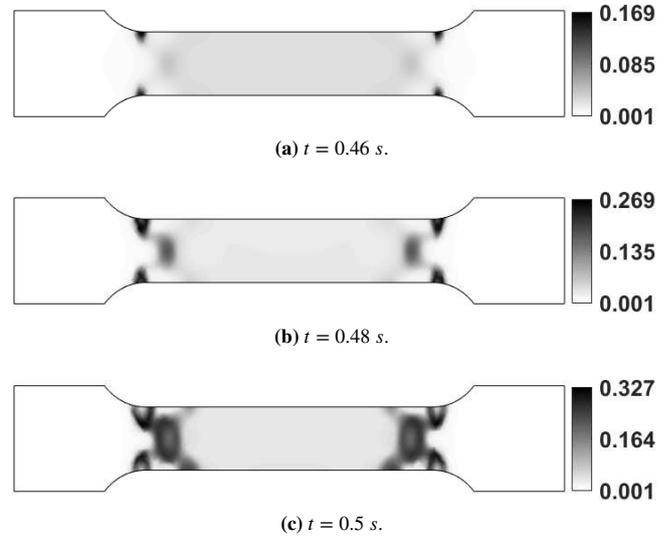
FIGURE 14 Damage phase-field deviation taking taking all parameters in ξ as random inputs. We have regions of uncertainty around all 4 points of possible crack initiation. At final time, the the uncertainty vanished where the crack propagated, and the maximum deviation around the crack is more than 30% of maximum damage.

points in each dimension. Unlike the notched case, here we have different expected locations for crack initiation that propagate from the surface to the interior of the body following the stress field concentration. Moreover, the final uncertainty in this case is more than 30% of the maximum damage, higher than any value from the notched case.

Figure 15 shows the stochastic sensitivity fields for all parameters on the tensile test case using 8 PCM points to compute the expected sensitivity. We can observe that 3 parameters are more sensitive, namely γ, g_c and a, and their absolute range are

(a) Phase-field layer width γ.

(b) Griffith fracture energy g_c.

(c) Rate of change of fatigue a.

(d) Viscous damping b.

(e) Rate of change of damage c.
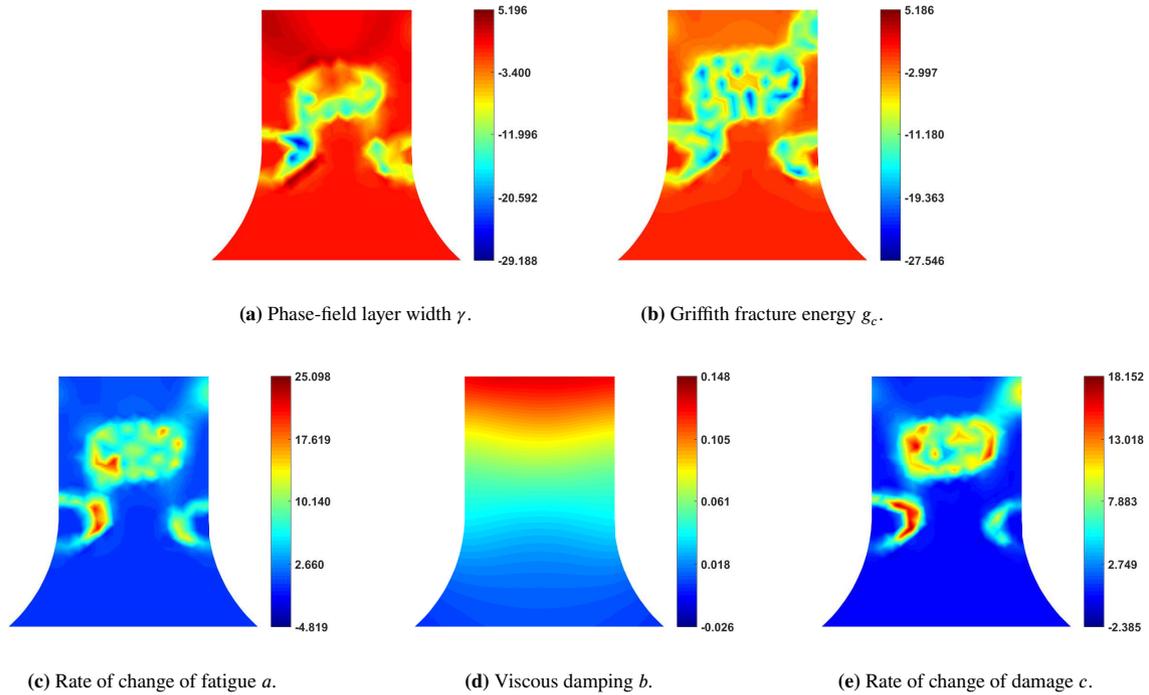
FIGURE 15 Local sensitivity expectation fields with respect to each input parameter. γ, g_c and a are the most sensitive parameters, with the same absolute range. b is not sensitive in the range considered and c is less sensitive than in the notched case.

equivalent, going from 5 to 30, approximately. We can argue that, since we do not have a preferential crack path nor a specific crack initiation position, all the uncertain parameters have the same sensitivity. The c parameter in this case is not as sensitive compared to the notched geometry, since here the crack location and path are not defined, so damage increase rate becomes less important compared to crack position. Last, we can see that b has little sensitivity on damage field in this case.

Another observation is that, contrary to the notched case, here the sensitivity of γ around the crack is negative, being positive elsewhere. Since we do not have a defined crack path, the increase of diffusion coefficient should smoothen the field. In other words, this case makes the γ associated with the Laplacian in the damage equation more sensitive than γ parameters in the remaining terms.

We present the total uncertainty field and sensitivity indices S_j for the tensile test specimen in Figure 16. Similarly to the notched case, here we see that the order of most influential parameters to the uncertainty regions are equivalent to the most sensitive parameters from Figure 15. In the regions of high uncertainty around the possible crack paths, the deviation field is influenced most by γ and g_c. Fatigue parameter a comes next, with relatively less importance than what was found in the local sensitivity analysis. Viscous damping b has little participation in total variance, while damage rate c has less importance when compared to the notched case. In summary, participation in regions of high uncertainty is dominated by γ and g_c.

Total sensitivity indices S_T^j for tensile specimen are presented in Figure 17. We can observe that when we include interactions between the parameters, a, b and c present sensitivity fields that are almost uniform between 0.44 and 0.5. The other 2 parameters, γ and g_c also present uniform fields, except for the regions around the crack where the total sensitivity indices are higher than 0.6.

From these examples it is clear that geometry and the existence of initial cracks, notches or singularities in the geometry plays an important role on sensitivity and uncertainty. In the notched case, the existence of a crack and the application of tensile stress makes the crack propagate straight to the right. The only uncertainty remains with the speed of damage increase ahead of the crack path, hence the sensitivities of g_c and c.

In the tensile specimen without notch on singularity, the uncertainty is driven by γ, g_c and a. From Equation 1, γ and g_c are multiplying the local interaction term, namely $g_c \frac{\gamma}{2}|\nabla\varphi|^2$ which later becomes the Laplacian in damage evolution, $\frac{\gamma(\omega)g_c(\omega)}{\lambda}\Delta\varphi$. Moreover, they are also associated with the tensor product on the equation of motion, also originated from the local interaction, and are associated to fatigue potentials $\mathcal{H}$ and $\mathcal{H}_f$, arbitrarily chosen. The complete symmetry of the tensile specimen geometry with no surface roughness or material imperfections, associated with the local operators and *ad hoc* modeling, leads to potential

(a) Total deviation field.

(b) Phase-field layer width γ.

(c) Griffith fracture energy g_c.

(d) Rate of change of fatigue a.

(e) Viscous damping b.

(f) Rate of change of damage c.
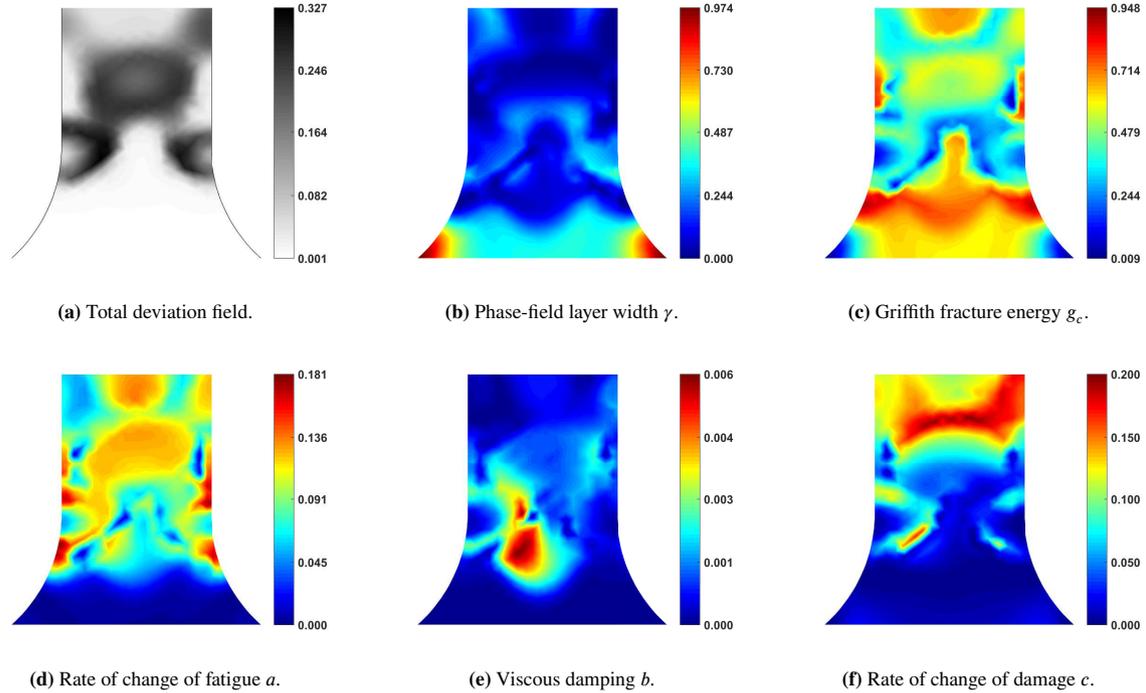
FIGURE 16 Tensile test specimen total damage deviation field and sensitivity indices (S^j) fields for all parameters using 6 points in each dimension at final time $T = 0.5\ s$. Differently than in the notched case, here γ and g_c are the most influential parameters in the region of higher uncertainty.

crack appearances in the 4 stress concentration regions around the fillets. Any numerical effect such as artificial damping or residuals may lead to perturbation in the solution and crack initiation at any corner.

Furthermore, the traditional disregard of nonlocal interactions in phase-field models excludes the possibility of modeling many phenomena experimentally observed, such as intermittent dislocation avalanches [27,28,29,30] and fractal characteristics of fracture [31,32], which show scale-free distributions and power-law scaling, that can be successfully modeled through fractional calculus [33]. Recent works have addressed fractional-order Cahn-Hilliard equation [34,35]. Phase-field models derived from free-energy potentials with nonlocal effects were first discussed by Giacomin and Lebowitz [36,37] with recent contributions from Abels et al [38], and Ainsworth and Mao [35]. Fractional-order models for structural analysis have been developed [39], to which corresponding fractional uncertainty/sensitivity analyses can be formulated via operator-based uncertainty quantification [40] and Fractional Sensitivity Equation Method (FSEM) [41].

5 | CONCLUSIONS

We developed an uncertainty quantification and sensitivity analysis framework for stochastic damage and fatigue phase-field equations. We used Monte Carlo sampling and Probabilistic Collocation to compute expectation and standard deviation of damage field, and expected local sensitivity. To compute the local sensitivity at each collocation point, complex-step differentiation was used. Probabilistic Collocation method poses a great advantage over random sampling methods such as MC, reducing significant computational costs with a simple implementation.

We presented two representative examples to study the uncertainty propagation in the model. We detected two different behaviors of the model based on geometry:

- In the single-edge notched tensile test case, where we already know the crack location and direction, the uncertainty is reduced to the speed of crack propagation. Interestingly, that is not only controlled by the rate of change of damage parameter c, but also indirectly by the Griffith energy g_c. Uncertainty can be inferred by local sensitivity analysis, which shows the same order of parameter influence. When we compute the global sensitivity indices, uncertainty around the crack tip is also controlled by g_c and c;

(a) Total deviation field.

(b) Phase-field layer width γ.

(c) Griffith fracture energy g_c.

(d) Rate of change of fatigue a.

(e) Viscous damping b.

(f) Rate of change of damage c.
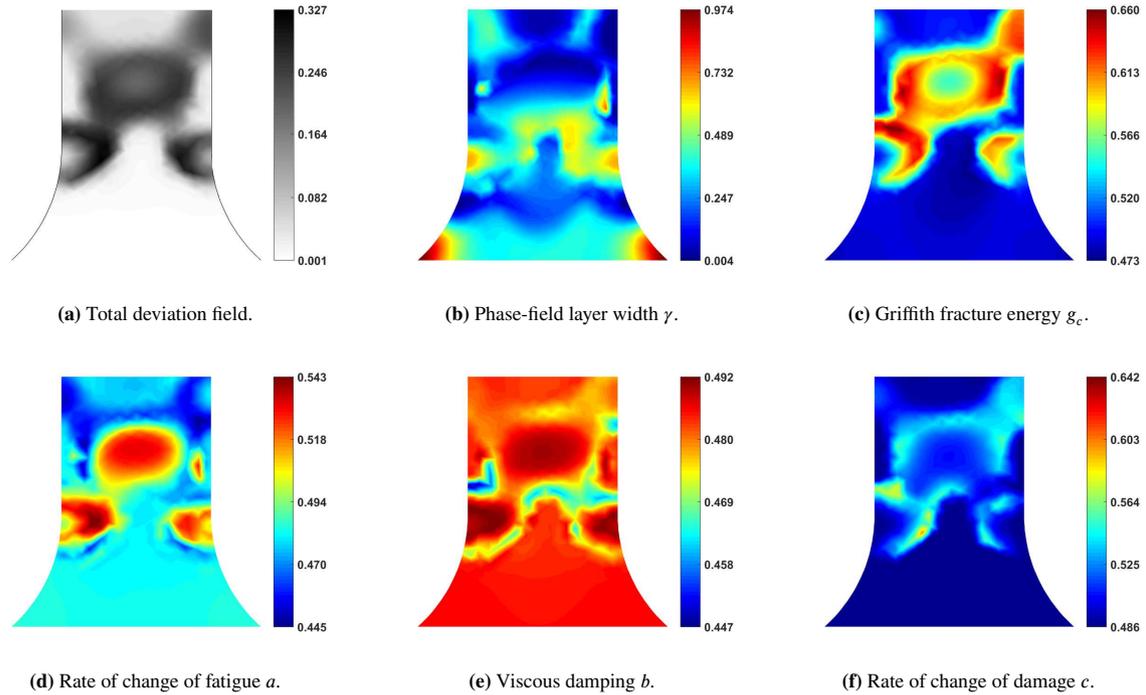
FIGURE 17 Tensile test specimen total damage deviation field and total effect sensitivity indices (S_T^j) fields for all parameters using 6 points in each dimension at final time $T = 0.5$ s. With the combined effect of all parameters, we still have γ and g_c as having most influence in the uncertainty regions.

- In a geometry with no unique crack initiation location nor a determined crack path, such as the tensile test specimen, fatigue coefficient a, and most importantly g_c and γ are the most sensitive parameters. High uncertainty is dominated by influence of g_c and γ, which help determine speed and mostly direction of damage transport, due to the lack of unique and well-known crack path.

The framework has shown that in undefined crack path or location, uncertainty is concentrated around parameters involved with local interactions. Specifically, γ and g_c are multiplying the local interaction term in the free-energy potential, and affect the equation of motion, the Laplacian in damage evolution and are also related to fatigue potentials, which are chosen arbitrarily. The higher sensitivity and uncertainty of those parameters related to local terms motivate the use of different operators that include nonlocal interactions as a way to mitigate model form uncertainty.

ACKNOWLEDGMENTS

☐

APPENDIX

A FINITE ELEMENT OPERATORS

From the semi-discrete system of equations (7), the solution at each element is written as a linear combination of local nodal basis functions such that

$$\mathbf{u}^k = \mathbf{N}^k \, \hat{\mathbf{u}}^k, \quad \text{(A1)} \qquad \mathbf{v}^k = \mathbf{N}^k \, \hat{\mathbf{v}}^k, \quad \text{(A2)} \qquad \boldsymbol{\varphi}^k = \mathbf{N}_\varphi^k \, \hat{\varphi}^k, \quad \text{(A3)} \qquad \mathcal{F}^k = \mathbf{N}_{\mathcal{F}}^k \, \hat{\mathcal{F}}^k, \quad \text{(A4)}$$

Constructing a mesh of linear triangles, the nodal solutions are defined as:

$$\hat{\mathbf{u}}^k = \begin{bmatrix} u_{1x}^k & u_{1y}^k & u_{2x}^k & u_{2y}^k & u_{3x}^k & u_{3y}^k \end{bmatrix}^T, \tag{A5}$$

$$\hat{\mathbf{v}}^k = \begin{bmatrix} v_{1x}^k & v_{1y}^k & v_{2x}^k & v_{2y}^k & v_{3x}^k & v_{3y}^k \end{bmatrix}^T, \tag{A6}$$

$$\hat{\boldsymbol{\varphi}}^k = \begin{bmatrix} \varphi_1^k & \varphi_2^k & \varphi_3^k \end{bmatrix}^T, \tag{A7}$$

$$\hat{\mathcal{F}}^k = \begin{bmatrix} \mathcal{F}_1^k & \mathcal{F}_2^k & \mathcal{F}_3^k \end{bmatrix}^T \tag{A8}$$

$$\tag{A9}$$

with interpolation matrices

$$\mathbf{N}^k = \begin{bmatrix} N_1 & 0 & N_2 & 0 & N_3 & 0 \\ 0 & N_1 & 0 & N_2 & 0 & N_3 \end{bmatrix}, \tag{A10}$$

$$\mathbf{N}_\varphi^k = \mathbf{N}_{\mathcal{F}}^k = \begin{bmatrix} N_1 & N_2 & N_3 \end{bmatrix}, \tag{A11}$$

$$\tag{A12}$$

Gradients of displacement, velocity and damage are approximated by linear combinations of shape function derivatives

$$\mathbf{E}^k = \mathbf{B}_u^k \, \hat{\mathbf{u}}^k, \quad \text{(A13)} \qquad \mathbf{D}^k = \mathbf{B}_v^k \, \hat{\mathbf{v}}^k, \quad \text{(A14)} \qquad \nabla \boldsymbol{\varphi}^k = \mathbf{B}_\varphi^k \, \hat{\varphi}^k, \quad \text{(A15)}$$

Derivative matrices are defined as:

$$\mathbf{B}_u^k = \begin{bmatrix} N_{1,x} & 0 & N_{2,x} & 0 & N_{3,x} & 0 \\ 0 & N_{1,y} & 0 & N_{2,y} & 0 & N_{3,y} \\ N_{1,y} & N_{1,x} & N_{2,y} & N_{2,x} & N_{3,y} & N_{3,x} \end{bmatrix}, \tag{A16}$$

$$\mathbf{B}_v^k = \begin{bmatrix} N_{1,x} & 0 & N_{2,x} & 0 & N_{3,x} & 0 \\ 0 & N_{1,y} & 0 & N_{2,y} & 0 & N_{3,y} \\ \frac{1}{\sqrt{2}}N_{1,y} & \frac{1}{\sqrt{2}}N_{1,x} & \frac{1}{\sqrt{2}}N_{2,y} & \frac{1}{\sqrt{2}}N_{2,x} & \frac{1}{\sqrt{2}}N_{3,y} & \frac{1}{\sqrt{2}}N_{3,x} \end{bmatrix}, \tag{A17}$$

$$\mathbf{B}_\varphi^k = \begin{bmatrix} N_{1,x} & N_{2,x} & N_{3,x} \\ N_{1,y} & N_{2,y} & N_{3,y} \end{bmatrix}. \tag{A18}$$

From those definitions, we can express the mass, stiffness and remaining operator matrices from Equation (7) as

$$\mathbf{M}^k = \int_{\Omega^k} \mathbf{N}^T \mathbf{N} d\Omega^k \, ; \tag{A19}$$

$$\mathbf{M}_\varphi^k = \int_{\Omega^k} \mathbf{N}_\varphi^T \mathbf{N}_\varphi \, d\Omega^k \, ; \tag{A20}$$

$$\mathbf{M}_{\mathcal{F}}^k = \int_{\Omega^k} \mathbf{N}_{\mathcal{F}}^T \mathbf{N}_{\mathcal{F}} \, d\Omega^k \, ; \tag{A21}$$

$$\mathbf{K}_u^k = -\int_{\Omega^k} \frac{1}{\rho_0} \left(1 - \mathbf{N}_\varphi^k \hat{\boldsymbol{\varphi}}^k\right)^2 \left(\mathbf{B}_u^k\right)^T C \mathbf{B}_u^k \, d\Omega^k \, ; \tag{A22}$$

$$\mathbf{K}_v^k = -\int_{\Omega^k} \frac{b}{\rho_0} \left(\mathbf{B}_v^k\right)^T \mathbf{B}_v^k \, d\Omega^k \, ; \tag{A23}$$

$$\mathbf{P}_\varphi^k = -\int_{\Omega^k} \frac{\gamma g_c}{\lambda} \left(\mathbf{B}_\varphi^k\right)^T \mathbf{B}_\varphi^k \, d\Omega^k - \int_{\Omega^k} \frac{g_c}{\lambda\gamma} \left(\mathbf{N}_\varphi^k\right)^T \mathbf{N}_\varphi^k \, d\Omega^k \, ; \tag{A24}$$

$$\mathbf{K}_c^k = -\int_{\Omega^k} \frac{1}{\lambda} \left(\mathbf{B}_u^k \hat{\mathbf{u}}^k\right)^T C \left(\mathbf{B}_u^k \hat{\mathbf{u}}^k\right) \left(\mathbf{N}_\varphi^k\right)^T \mathbf{N}_\varphi^k \, d\Omega^k \, ; \tag{A25}$$

$$\mathbf{w}_a^k = \int_{\Omega^k} \frac{\gamma g_c}{\rho_0} \left(\mathbf{B}_\varphi^k \hat{\boldsymbol{\varphi}}^k \otimes \mathbf{B}_\varphi^k \hat{\boldsymbol{\varphi}}^k\right) : \mathbf{B}_u^k \, d\Omega^k \, ; \tag{A26}$$

$$\mathbf{w}_b^k = \int_{\Omega^k} \frac{1}{\lambda} \left(\mathbf{B}_u^k \hat{\mathbf{u}}^k\right)^T C \left(\mathbf{B}_u^k \hat{\mathbf{u}}^k\right) \mathbf{N}_\varphi^k \, d\Omega^k \, ; \tag{A27}$$

$$\mathbf{w}_c^k = \int_{\Omega^k} \frac{-1}{\lambda\gamma} \left(\mathbf{N}_{\mathcal{F}}^k\right)^T \mathbf{N}_{\mathcal{F}}^k \hat{\mathcal{F}}^k \, d\Omega^k \, ; \tag{A28}$$

$$\mathbf{w}_d^k = \int_{\Omega^k} \frac{a}{\gamma} \left(1 - \mathbf{N}_\varphi^k \hat{\boldsymbol{\varphi}}^k\right) \left(\mathbf{N}_\varphi^k \hat{\boldsymbol{\varphi}}^k\right) \left|\left[C \left(\mathbf{B}_u^k \hat{\mathbf{u}}^k\right) + b \left(\mathbf{B}_v^k \hat{\mathbf{v}}^k\right)\right] : \left(\mathbf{B}_v^k \hat{\mathbf{v}}^k\right)\right| d\Omega^k \, . \tag{A29}$$

We consider the plane stress elasticity matrix C given by

$$C = \frac{E}{1 - \nu^2} \begin{bmatrix} 1 & \nu & 0 \\ \nu & 1 & 0 \\ 0 & 0 & \frac{(1-\nu)}{2} \end{bmatrix} \tag{A30}$$

We express the second-order tensor in Equation A26 as a vector using Voigt notation.

B NEWMARK INTEGRATION METHOD

From Equation (7) we consider the semi-discrete equation of motion with suitable initial and boundary conditions for displacement $\mathbf{u}$, velocity $\dot{\mathbf{u}}$ and acceleration $\ddot{\mathbf{u}}$. In Newmark scheme, acceleration and velocity at time t_{n+1} are approximated by

$$\ddot{\mathbf{u}}_{n+1} = \alpha_1 \left(\mathbf{u}_{n+1} - \mathbf{u}_n\right) - \alpha_2 \dot{\mathbf{u}}_n - \alpha_3 \ddot{\mathbf{u}}_n \tag{B31}$$

$$\dot{\mathbf{u}}_{n+1} = \alpha_4 \left(\mathbf{u}_{n+1} - \mathbf{u}_n\right) + \alpha_5 \dot{\mathbf{u}}_n + \alpha_6 \ddot{\mathbf{u}}_n, \tag{B32}$$

with $\alpha_i, i = 1, 2, \ldots, 6$ written in terms of standard Newmark coefficients $\tilde{\gamma}$ and $\tilde{\beta}$:

$$\alpha_1 = \frac{1}{\tilde{\beta}\Delta t^2}, \ \alpha_2 = \frac{1}{\tilde{\beta}\Delta t}, \ \alpha_3 = \frac{1 - 2\tilde{\beta}}{2\tilde{\beta}}, \ \alpha_4 = \frac{\tilde{\gamma}}{\tilde{\beta}\Delta t}, \ \alpha_5 = 1 - \frac{\tilde{\gamma}}{\tilde{\beta}} \ \text{and} \ \alpha_6 = \left(1 - \frac{\tilde{\gamma}}{2\tilde{\beta}}\right)\Delta t. \tag{B33-B38}$$

References

1. Lemaitre J, Desmorat R. *Engineering damage mechanics: ductile, creep, fatigue and brittle failures*. Springer Science & Business Media . 2005.

2. Anderson TL. *Fracture mechanics: fundamentals and applications*. CRC press . 2017.

3. Kanninen MF, Popelar CL. *Advanced fracture mechanics* . 1985.

4. Cahn JW, Hilliard JE. Free Energy of a Nonuniform System. I. Interfacial Free Energy. *The Journal of Chemical Physics* 1958; 28(2): 258–267.

5. Allen SM, Cahn JW. A microscopic theory for antiphase boundary motion and its application to antiphase domain coarsening. *Acta Metallurgica* 1979; 27(6): 1085–1095.

6. Lima EABF, Oden JT, Almeida RC. A hybrid ten-species phase-field model of tumor growth. *Mathematical Models and Methods in Applied Sciences* 2014; 24(13): 2569–2599.

7. Yue P, Feng JJ, Liu C, Shen J. A diffuse-interface method for simulating two-phase flows of complex fluids. *Journal of Fluid Mechanics* 2004; 515: 293âĂŞ317.

8. Sun P, Xu J, Zhang L. Full Eulerian finite element method of a phase field model for fluidâĂŞstructure interaction problem. *Computers & Fluids* 2014; 90: 1 – 8.

9. Miehe C, Hofacker M, Welschinger F. A phase field model for rate-independent crack propagation: Robust algorithmic implementation based on operator splits. *Computer Methods in Applied Mechanics and Engineering* 2010; 199(45-48): 2765–2778.

10. Miehe C, Welschinger F, Hofacker M. Thermodynamically consistent phase-field models of fracture: Variational principles and multi-field FE implementations. *International Journal for Numerical Methods in Engineering* 2010; 83(10): 1273–1311.

11. Borden MJ, Hughes TJ, Landis CM, Verhoosel CV. A higher-order phase-field model for brittle fracture: Formulation and analysis within the isogeometric analysis framework. *Computer Methods in Applied Mechanics and Engineering* 2014; 273: 100–118.

12. Ambati M, Gerasimov T, De Lorenzis L. Phase-field modeling of ductile fracture. *Computational Mechanics* 2015; 55(5): 1017–1040.

13. Ambati M, Kruse R, De Lorenzis L. A phase-field model for ductile fracture at finite strains and its experimental verification. *Computational Mechanics* 2016; 57(1): 149–167.

14. Borden MJ, Verhoosel CV, Scott MA, Hughes TJ, Landis CM. A phase-field description of dynamic brittle fracture. *Computer Methods in Applied Mechanics and Engineering* 2012; 217-220: 77–95.

15. Hofacker M, Miehe C. A phase field model of dynamic fracture: Robust field updates for the analysis of complex crack patterns:. *International Journal for Numerical Methods in Engineering* 2013; 93(3): 276–301.

16. Amendola G, Fabrizio M, Golden JM. Thermomechanics of damage and fatigue by a phase field model. *Journal of Thermal Stresses* 2016; 39(5): 487–499.

17. Caputo M, Fabrizio M. Damage and fatigue described by a fractional derivative model. *Journal of Computational Physics* 2015; 293: 400–408.

18. Boldrini J, Barros de Moraes E, Chiarelli L, Fumes F, Bittencourt M. A non-isothermal thermodynamically consistent phase field framework for structural damage and fatigue. *Computer Methods in Applied Mechanics and Engineering* 2016; 312: 395–427.

19. Chiarelli L, Fumes F, Barros de Moraes E, Haveroth G, Boldrini J, Bittencourt M. Comparison of high order finite element and discontinuous Galerkin methods for phase field equations: Application to structural damage. *Computers & Mathematics with Applications* 2017; 74(7): 1542–1564.

20. Haveroth G, Barros de Moraes E, Boldrini J, Bittencourt M. Comparison of semi and fully-implicit time integration schemes applied to a damage and fatigue phase field model. *Latin American Journal of Solids and Structures* 2018; 15(5): 1-16.

21. Hamdia KM, Msekh MA, Silani M, et al. Uncertainty quantification of the fracture properties of polymeric nanocomposites based on phase field modeling. *Composite Structures* 2015; 133: 1177–1190.

22. Lima EABF, Almeida RC, Oden JT. Analysis and numerical solution of stochastic phase-field models of tumor growth: Stochastic Tumor Growth. *Numerical Methods for Partial Differential Equations* 2015; 31(2): 552–574.

23. Martins JR, Sturdza P, Alonso JJ. The complex-step derivative approximation. *ACM Transactions on Mathematical Software (TOMS)* 2003; 29(3): 245–262.

24. Saltelli A, Annoni P, Azzini I, Campolongo F, Ratto M, Tarantola S. Variance based sensitivity analysis of model output. Design and estimator for the total sensitivity index. *Computer Physics Communications* 2010; 181(2): 259–270.

25. Smolyak SA. Quadrature and interpolation formulas for tensor products of certain classes of functions. In: . 148. Russian Academy of Sciences. ; 1963: 1042–1045.

26. Sobol IM. Sensitivity estimates for nonlinear mathematical models. *Mathematical modelling and computational experiments* 1993; 1(4): 407–414.

27. Miguel MC, Vespignani A, Zapperi S, Weiss J, Grasso JR. Intermittent dislocation flow in viscoplastic deformation. *Nature* 2001; 410(6829): 667–671.

28. Weiss J. Three-Dimensional Mapping of Dislocation Avalanches: Clustering and Space/Time Coupling. *Science* 2003; 299(5603): 89–92.

29. Koslowski M, LeSar R, Thomson R. Avalanches and Scaling in Plastic Deformation. *Physical Review Letters* 2004; 93(12).

30. Richeton T, Weiss J, Louchet F. Breakdown of avalanche critical behaviour in polycrystalline plasticity. *Nature Materials* 2005; 4(6): 465–469.

31. Mandelbrot BB, Passoja DE, Paullay AJ. Fractal character of fracture surfaces of metals. *Nature* 1984; 308: 721.

32. Hähner P, Bay K, Zaiser M. Fractal Dislocation Patterning During Plastic Deformation. *Physical Review Letters* 1998; 81(12): 2470–2473. doi: 10.1103/PhysRevLett.81.2470

33. Carpinteri A, Mainardi F. *Fractals and fractional calculus in continuum mechanics*. 378. Springer . 2014.

34. Ainsworth M, Mao Z. Analysis and Approximation of a Fractional Cahn–Hilliard Equation. *SIAM Journal on Numerical Analysis* 2017; 55(4): 1689–1718.

35. Ainsworth M, Mao Z. Well-posedness of the Cahn–Hilliard equation with fractional free energy and its Fourier Galerkin approximation. *Chaos, Solitons & Fractals* 2017; 102: 264–273.

36. Giacomin G, Lebowitz JL. Phase segregation dynamics in particle systems with long range interactions. I. Macroscopic limits. *Journal of Statistical Physics* 1997; 87(1-2): 37–61.

37. Giacomin G, Lebowitz JL. Phase Segregation Dynamics in Particle Systems with Long Range Interactions II: Interface Motion. *SIAM Journal on Applied Mathematics* 1998; 58(6): 1707–1729.

38. Abels H, Bosia S, Grasselli M. Cahn–Hilliard equation with nonlocal singular free energies. *Annali di Matematica Pura ed Applicata (1923 -)* 2015; 194(4): 1071–1106.

39. Suzuki J, Zayernouri M, Bittencourt M, Karniadakis G. Fractional-order uniaxial visco-elasto-plastic models for structural analysis. *Computer Methods in Applied Mechanics and Engineering* 2016; 308: 443–467.

40. Kharazmi E, Zayernouri M. Operator-Based Uncertainty Quantification of Stochastic Fractional PDEs. *arXiv preprint arXiv:1806.00110* 2018.

41. Kharazmi E, Zayernouri M. Fractional Sensitivity Equation Method: Applications to Fractional Model Construction. *arXiv preprint arXiv:1806.00477* 2018.